ACS APPLIED MATERIALS & INTERFACES

www.acsami.org

Research Article

# Antibacterial, Antiviral, and Self-Cleaning Mats with Sensing Capabilities Based on Electrospun Nanofibers Decorated with ZnO Nanorods and Ag Nanoparticles for Protective Clothing Applications

Sultan Karagoz, N. Burak Kiremitler, Gokhan Sarp, Sami Pekdemir, Samaa Salem, Ayşe Gencay Goksu, M. Serdar Onses, Ibrahim Sozdutmaz, Ertugrul Sahmetlioglu, Ergun Samet Ozkara, Ahmet Ceylan, and Erkan Yilmaz*

Cite This: *ACS Appl. Mater. Interfaces* 2021, 13, 5678–5690

Read Online

ACCESS | Metrics & More | Article Recommendations | Supporting Information

**ABSTRACT:** The COVID-19 pandemic has clearly shown the importance of developments in fabrication of advanced protective equipment. This study investigates the potential of using multifunctional electrospun poly(methyl methacrylate) (PMMA) nanofibers decorated with ZnO nanorods and Ag nanoparticles (PMMA/ZnO−Ag NFs) in protective mats. Herein, the PMMA/ZnO−Ag NFs with an average diameter of 450 nm were simply prepared on a nonwoven fabric by directly electrospinning from solutions containing PMMA, ZnO nanorods, and Ag nanoparticles. The novel material showed high performance with four functionalities (i) antibacterial agent for killing of Gram-negative and Gram-positive bacteria, (ii) antiviral agent for inhibition of corona and influenza viruses, (iii) photocatalyst for degradation of organic pollutants, enabling a self-cleaning protective mat, and (iv) reusable surface-enhanced Raman scattering substrate for quantitative analysis of trace pollutants on the nanofiber. This multi-functional material has high potential for use in protective clothing applications by providing passive and active protection pathways together with sensing capabilities.

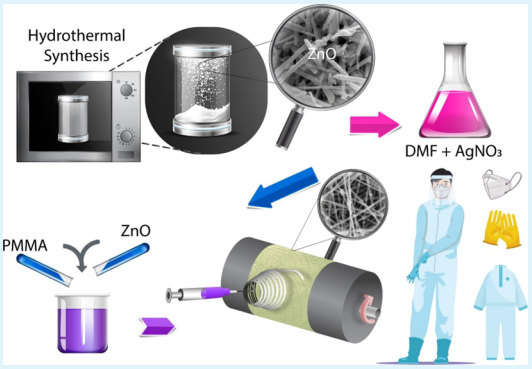


**KEYWORDS:** *protective clothing, electrospun nanofibers, ZnO nanorods, silver nanoparticles, photocatalytic degradation, antiviral activity, antibacterial activity, SERS*



## 1. INTRODUCTION

Multi-functional materials with antiviral, antibacterial, photocatalytic, and sensing properties are of great interest for applications in health care settings. A particularly important application of such materials is in personal protective equipment. Especially in pandemic situations, where it is difficult to access protective equipment, it is vital to use functional mats that can keep viral contamination to a minimum and for which they can be used for a long time due to their self-cleaning ability. The 2019 coronovirus outbreak (COVID-19) has clearly shown the need for substantial developments in personal protective equipment. An ideal protective mat should be self-cleanable, provide resistance against bacteria and virus infections, and at the same time should allow for direct investigation of the pollutant molecules. Multi-functional materials with antiviral, antibacterial, photocatalytic, and surface-enhanced Raman scattering (SERS) activities can enable such functionalities, provided that they are seamlessly integrated into conventional textiles without loss of their inherently advantageous properties such as porous structure, flexibility, and light weight.[1−3]

Metals and their compounds have been recently demonstrated to be efficient against a wide range of pathogens including viruses, bacteria, and fungus. Among metal species, Zn can exert antiviral and antibacterial activities against pathogens that cause disease in humans.[4] In view of the emerging COVID-19 pandemic caused by the novel coronavirus, SARS-CoV-2, the study of Zn with potential antiviral effects is of particular and urgent interest.[5] The antiviral mechanism of action of Zn is usually defined as adhering to one of the following models: inhibition of virus replication, reducing the activity of angiotensin-converting enzyme 2 (ACE2), conditional upregulation of IFN-$\alpha$ (interferon $\alpha$), inhibition of nuclear factor-kappa B (NF-$\kappa$B) with an immunologic role, acting as a cofactor for numerous viral proteins, preventing the entry of the virus from the cell

Received: August 30, 2020
Accepted: January 15, 2021
Published: January 25, 2021




https://dx.doi.org/10.1021/acsami.0c15606
*ACS Appl. Mater. Interfaces* 2021, 13, 5678−5690

membrane, reduction of the risk of bacterial coinfection by improving direct antibacterial effects against *Streptococcus pneumoniae*. However, additional clinical studies and extensive experimental data are needed in this area.[5,6] In fact, ZnO and Ag are extensively used in antibacterial studies. Although the antibacterial activity of a single ZnO nanomaterial is relatively weak, modifying ZnO with metals can produce very strong antibacterial activity.[7] Moreover, it was shown that Ag inactivates both Gram-positive and Gram-negative bacteria. Nevertheless, it is more effective against Gram (−) bacteria. This difference can be attributed to larger peptidoglycan content in the cell membrane of Gram (+) bacteria.[8] Recently, the ZnO/Ag hybrid nanocomposite has been reported to exhibit significant antibacterial activity against various microorganisms.[9] The mechanism of their antimicrobial activity is represented by the induction of release of reactive oxygen species (ROS), disturbance of the function of proteins and DNA, and disruption of the bacterial cell membrane.[10,11]

The COVID-19 pandemic has clearly shown the importance of protective materials with advanced capabilities. The studies for the production of multifunctional mats have gained increasing attention for protective clothing applications. The photocatalytic degradation of organic pollutants, viruses, and bacteria on photocatalytic active surfaces such as $TiO_2$, ZnO, ZnS, and $Bi_2WO_6$ is an effective way of self-cleaning of materials modified with these particles under light.[12−14] As a result of the modification of the protective mats with photocatalytic active particles, the ability to self-clean under light is an important alternative for repeated use of protective clothing.

A highly critical but missing capability is direct sensing of molecules deposited on the protective mats. This kind of sensing can enable monitoring the degree of contamination of the environment and also inform about the health status of the individual. A powerful, rapid, and label-free technique for analysis of molecules is Raman spectroscopy. The weak inelastic scattering of light from a low concentration of molecules is a practical barrier toward its use for probing mats. SERS overcomes this challenge by using plasmonic nanoparticles that boost the signal several orders of magnitude. Therefore, protective mats should be decorated with plasmonic nanoparticles for electromagnetic enhancement of the signals from the molecules. Based on the previous research on direct detection of viruses via Raman spectroscopy, it may even be possible to perform diagnosis of COVID-19 simply by analyzing protective mats.[12−15]

In this study, we report a practical method to prepare multifunctional mats for modification of protective clothing by direct electrospinning of NFs decorated with ZnO nanorods and Ag nanoparticles. The fabrication is performed in one-step by electrospinning of poly(methyl methacrylate) (PMMA) solutions containing ZnO nanorods and Ag nanoparticles. The structural, antiviral, antibacterial, and photocatalytic properties and SERS performance of the PMMA/ZnO−Ag NF mats have been investigated. The results showed that the multifunctional material has antiviral, antibacterial, self-cleaning properties and SERS activity, and it may have the potential to be used in protective clothing applications.

## 2. EXPERIMENTAL SECTION

**2.1. Synthesis of ZnO Nanorods.** ZnO nanorods were synthesized by using the hydrothermal method. First, 2 g of $ZnCl_2$ (Merck, Darmstadt, Germany) was dissolved by being sonicated in distilled water (50 mL) and stirred for further 10 min. Thereafter, 5 g of sodium hydroxide (NaOH), purchased from Sigma-Aldrich (St. Louis, MO, USA), was added to the solution. After mixing for 10 min, the solutions were transferred into a Teflon-lined stainless-steel autoclave with a capacity of 100 mL. The hydrothermal synthesis was performed at 180 °C for 12 h in an oven. The obtained white products were separated from the solution by centrifugation and then washed with distilled water and ethanol several times. It was dried at 50 °C in an oven.

**2.2. Fabrication of PMMA/ZnO−Ag Nanofibers.** To prepare PMMA/ZnO−Ag NFs, ZnO nanorods (10 wt %) were first dispersed in 4 mL of *N*,*N*-dimethylformamide (DMF) (Sigma-Aldrich, St. Louis, MO, USA). Thereafter, Triton X-100 (Sigma-Aldrich) (5 wt %) as surfactant was added to prevent agglomeration and precipitation of the nanorods. The mixture was exposed to sequential ultrasonication for 20 min to disperse the ZnO nanoparticles. After obtaining a homogeneous mixture, PMMA ($M_w$ = 996,000 g/mol, 6 wt %) was mixed with the ZnO solution using a magnetic stirrer (1000 rpm). The solution was maintained under stirring for 3 h until the polymer was completely dissolved in DMF. Finally, different concentrations of silver nitrate ($AgNO_3$, ≥99.5%, Sigma-Aldrich) (0.5, 1, 3, 5 wt %) was added to the solution containing PMMA and ZnO nanorods in DMF. Afterward, the solution was kept under stirring overnight until its color turned to dark brown.

Fabrication of PMMA/ZnO−Ag NFs on mats was carried out by using a commercial electrospinning unit (Holmarc HO-NFES-040). The obtained solution was transferred into a 5 mL syringe having an 18 g metallic needle and the syringe was positioned horizontally against a grounded aluminum collector (75 mm in diameter and 200 mm in length) covered with the mat. During the electrospinning process, the following parameters were used: needle to collector distance of 15 cm, applied voltage of 13 kV, and flow rate of 0.5 mL/h. When the solution reached the tip of the needle, NFs were electrospun on the rotating collector (600 rpm).

**2.3. Antimicrobial Activity Assays.** The antimicrobial activity of the PMMA/ZnO−Ag NF mat was determined by the agar disc diffusion method. Bacterial strains *Escherichia coli* (*E. coli*) (ATCC 25922) and *Staphylococcus aureus* (*S. aureus*) (ATCC 25923) are examples of Gram-negative and Gram-positive class of bacteria, respectively, and were used for the antibacterial activity assessment. The bacteria were cultured overnight at 37 °C in Muller−Hinton medium (Bio-Rad). The inocula of bacteria were prepared from 24 h broth cultures, and suspensions were adjusted to 0.5 McFarland. Suspensions of the tested microorganisms (100 μL of $10^7$ cells/mL) were spread over the surface of Petri dishes. PMMA/ZnO−Ag NFs on the mat were attached to filter paper discs of 6.0 mm diameter and placed on the inoculated agar plates. An empty disk was used as a negative control. The microorganisms were incubated at 37 °C for 24 h. A clear zone of inhibition observed after the incubation period was measured using a scale. All the assessments were performed in duplicate.

**2.4. Antiviral Activity Assays.** *2.4.1. Cell Culture and Virus Propagation.* The Madin−Darby bovine kidney epithelial (MDBK) cell line was used for virus cultivation and antiviral activity studies. The cells were cultured at 37 °C in 5% $CO_2$ in Dulbecco's modified Eagle's medium (DMEM, Sigma-Aldrich, St. Louis, MO, USA) supplemented with 10% fetal bovine serum (Hyclone), penicillin, streptomycin, and neomycin (Biological Industries). Two types of viruses were selected as a model for respiratory infections: bovine coronavirus (BCoV), an enveloped positive-sense single-stranded RNA virus, and bovine parainfluenza virus-3 (BPIV3), an enveloped negative sense single-stranded virus. Viruses were cultivated in the MDBK cell line and the $TCID_{50}$ (Tissue Culture Infectious Dose 50) virus titer was determined and stored in −80 °C until use.

*2.4.2. Evaluation of Antiviral Activity.* The antiviral activity test was carried out by modifying from a previously reported method.[14] Cells were seeded into 96-well plates at a density of approximately $10^4$ cells per well in 100 μL of culture medium and incubated at 37 °C and 5% $CO_2$ for 24 h. The sample was prepared by cutting mats with electrospun PMMA/ZnO−Ag NFs in a size of 10 × 10 $mm^2$. The


https://dx.doi.org/10.1021/acsami.0c15606
ACS Appl. Mater. Interfaces 2021, 13, 5678−5690

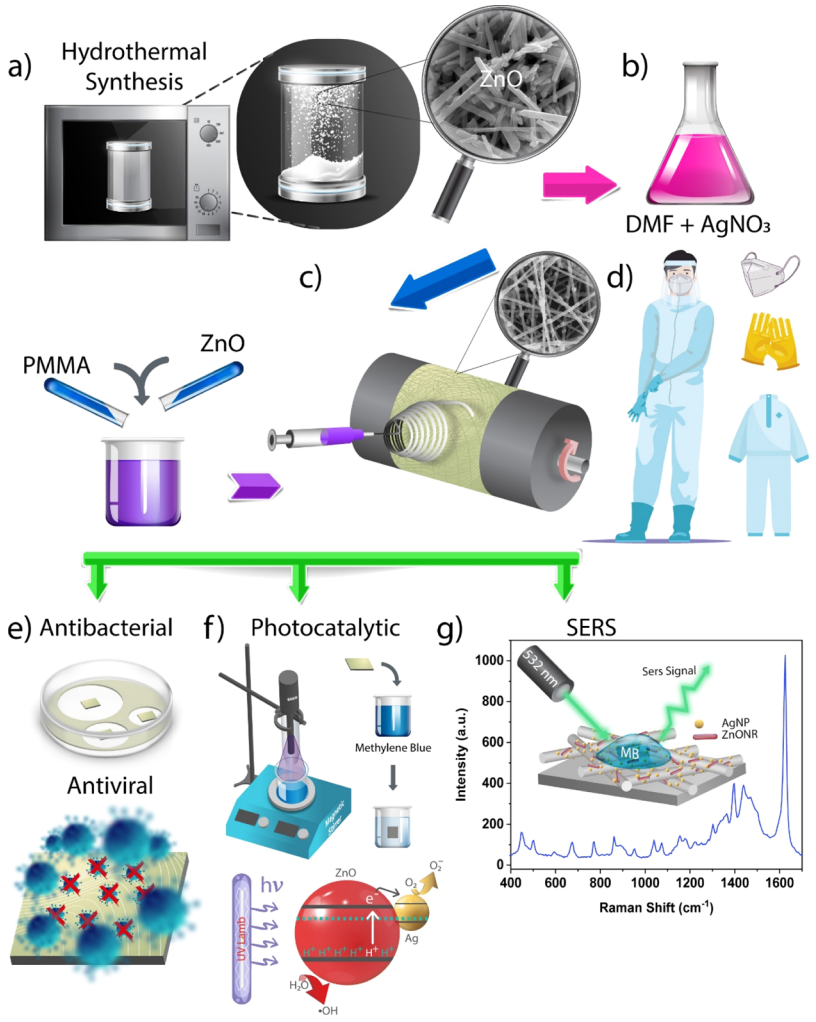


**Figure 1.** Fabrication steps of PMMA/ZnO−Ag NFs (a−d): (a) synthesis of ZnO nanorods by the hydrothermal method and SEM image of ZnO nanorods, (b) preparation of the electrospinning solution by mixing PMMA and ZnO nanorods with the solution of Ag NPs synthesized by in situ reduction of $AgNO_3$ in the presence of DMF, (c) fabrication of PMMA/ZnO−Ag NFs on a mat by electrospinning and integration of NF mats to use protective clothes, (d) schematic illustration of a protective clothing containing PMMA/ZnO−Ag NF mats, and (e−g) multifunctional properties of the fabricated of PMMA/ZnO−Ag NF mats.

concentration of NFs on the mat was 2 mg/cm$^2$. The calculated concentrations of ZnO nanorods and Ag NPs in NFs were 1 mg and 0.3 mg per area (1 cm$^2$), respectively. Samples with the NF layer were filled in a sterile centrifuge tube, and 100 $\mu$L of each virus with 1 × $10^8$ $TCID_{50}$/0.1 titer was added on. Each sample with virus solutions was incubated for 1 and 24 h at 24 °C. At the end of the incubation periods, 900 $\mu$L of DMEM was added to each sample and sample-virus dilutions were prepared from $10^{-8}$ to $10^{-1}$. Before inoculation of the cells, they were gently washed 2 times with PBS and 100 $\mu$L dilutions were added in quadruplet wells of the confluent monolayer of MDBK cells ($10^4$ cells/well) in a flat-bottomed 96-well microtiter plate and further incubated for 24 h. The same procedure was repeated for the untreated sample (mat without nanofibers) as a control group. Each well was examined for the presence of a cytopathic effect using an inverted optical microscope. Tests were repeated 3 times. The $TCKID_{50}$ values of viruses were calculated by the Spearman Karber method.[16]

The antiviral activity of PMMA/ZnO−Ag NFs was evaluated by the following equation

$$M_v = \log(V_b) - \log(V_c) \quad (1)$$

where $M_v$ represents antibacterial activity, $V_b$ represents $TCKID_{50}$ titer of the control sample, and $V_c$ is the $TCKID_{50}$ titer of the sample.

### 2.5. Photocatalytic Degradation and Self-Cleaning Studies.

The photocatalytic properties of the prepared PMMA/ZnO−Ag NFs were studied using methylene blue (MB) and 4-nitrophenol as probe molecules. The weight of NFs on the mat surface was about 250 mg for all different NFs. For this purpose, PMMA/ZnO−Ag NFs (100 × 100 mm) were immersed in a glass beaker with a volume capacity of 400 mL filled with 250 mL of aqueous solution of MB or 4-nitrophenol at a concentration of 10 mg·L$^{-1}$. The degradation of the probe molecules was performed by exposure to a UV irradiation source of 380 nm wavelength with a power of 400 W. The reaction solution (approximately ∼1.0 mL) was pipetted into a quartz cell and its absorption spectrum was measured every 20 min by using a UV−visible spectrophotometer. Analysis was carried out at 400 nm for 4-nitrophenol and 664 nm for MB, respectively.

The photocatalytic efficiency of PMMA/ZnO−Ag NFs was also studied by degradation of trimetrophim as a colorless probe contaminant and analysis was carried out by using a high-performance liquid chromatography diode array detection system (HPLC-DAD). A $C_{18}$ chromatography column (5 mm, 150 × 4.6 mm, Silur, USEM Research and Development Company, Turkey) was used for trimetrophim analysis in HPLC.

The percentage of the degradation ratio was calculated according to the following equations


https://dx.doi.org/10.1021/acsami.0c15606
ACS Appl. Mater. Interfaces 2021, 13, 5678−5690

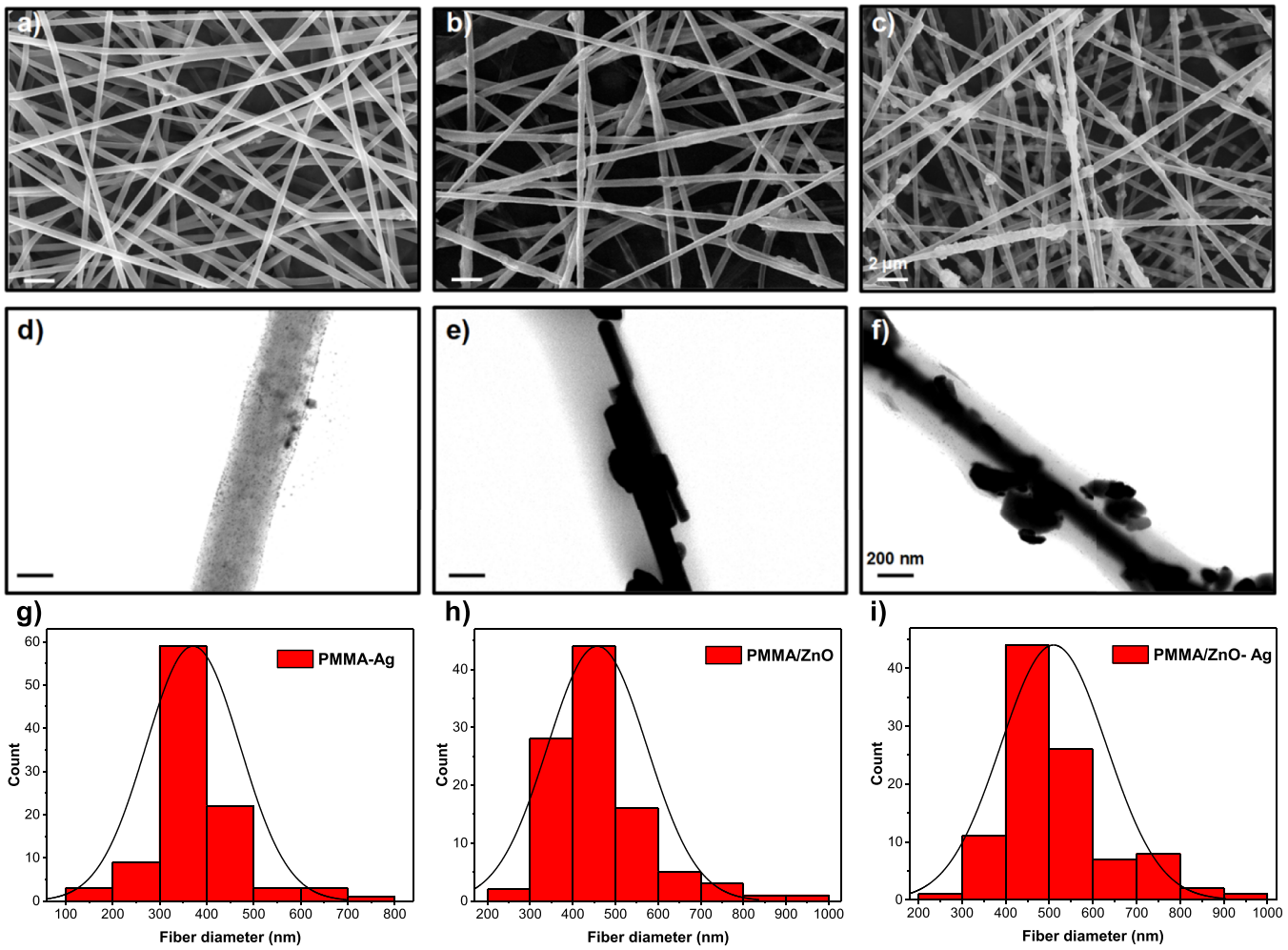


**Figure 2.** Morphology and diameter analysis of NF mats. SEM and STEM images of (a,d) PMMA/Ag, (b,e) PMMA/ZnO, and (c,f) PMMA/ZnO−Ag NF mats. Histogram of diameter distribution and average diameter of (g) PMMA/Ag, (h) PMMA/ZnO, and (i) PMMA/ZnO−Ag NF mats.

$$\text{degradation } \% = \frac{A_0 - A_t}{A_0} \tag{2}$$

where $A_0$ is the initial concentrations of the probe molecules and $A_t$ is the concentration of the probe molecules after ""$t$" min.

$$\ln\left(\frac{C_t}{C_0} = -kt\right) \tag{3}$$

Equation 3 represents the pseudo-first-order chemical kinetics reaction where $k$ ($\text{min}^{-1}$) is the reaction rate constant which was calculated from the slope of the regression line ($C_t/C_0$) as a function of irradiation time $t$. Thereby, $C_t$ and $C_0$ represent the concentration of probing molecules at the initial stage and the adsorption equilibrium concentration after being irradiated at an irradiation time $t$ (min), respectively.[17]

$$\ln 2 = Kt_{1/2} = 0.693 \tag{4}$$

where $t_{1/2}$ is the half time; it is defined as the time required for the initial concentration of the analyte to be reduced to one-half of its initial concentration value.

**2.6. SERS Measurements.** An Alpha $M^+$ Raman spectrometer (confocal micro-Raman microscope, Witec, Germany) was used to observe the SERS spectra of MB as a model organic probe molecule. The probe molecule was dissolved in water and drop-cast on PMMA/ZnO−Ag NFs with a volume of 2 $\mu$L and at a concentration of 1 mM. The SERS measurements were performed following evaporation of water at room temperature.[18] The Raman spectrometer system was configured with a laser line of 532 nm. The power of the laser was 0.1 mW. A fine-focusing 50× microscope objective (N.A. = 0.85) with a laser spot of 2 $\mu$m was used for the measurements. The Raman intensity mapping was performed at an integration time of 0.05 s on an area of 40 × 40 $\mu m^2$ with a step size of 0.5 $\mu$m. Raman mappings were generated based on the peak of MB at 1625 $cm^{-1}$. A baseline correction was performed for each spectrum. The detection limit of the substrate was determined using a 2 $\mu$L droplet of MB with a concentration that ranged from $10^{-3}$ to $10^{-9}$ M. The analytical enhancement factor (AEF) of the MB was calculated by the following eq 5[17]

$$\text{AEF} = \frac{I_{\text{SERS}}}{I_{\text{RM}}} \times \frac{C_{\text{RM}}}{C_{\text{SERS}}} \tag{5}$$

where the intensity of the Raman signal ($I_{\text{RM}}$) was obtained on a non-SERS substrate (pure PMMA NFs on fabric) with the concentration of analyte solution ($C_{\text{RM}}$) under non-SERS condition, and the intensity of SERS signal ($I_{\text{SERS}}$) was obtained on the SERS substrate with the concentration of analyte solution ($C_{\text{SERS}}$) under SERS condition. SERS was also measured by applying 4-nitrophenol at a concentration of 1 mM per $cm^2$ on the mat surface.

**2.7. Characterization.** The surface morphology of the as-prepared NFs was acquired by using a scanning electron microscope (Zeiss EVO LS10) at 25 kV and field emission scanning electron microscope in STEM mode (Zeiss Gemini 500) at 1 kV. For SEM imaging, NF mats were sputter-coated (Quorum 150R-ES) with a Au


https://dx.doi.org/10.1021/acsami.0c15606
ACS Appl. Mater. Interfaces 2021, 13, 5678−5690

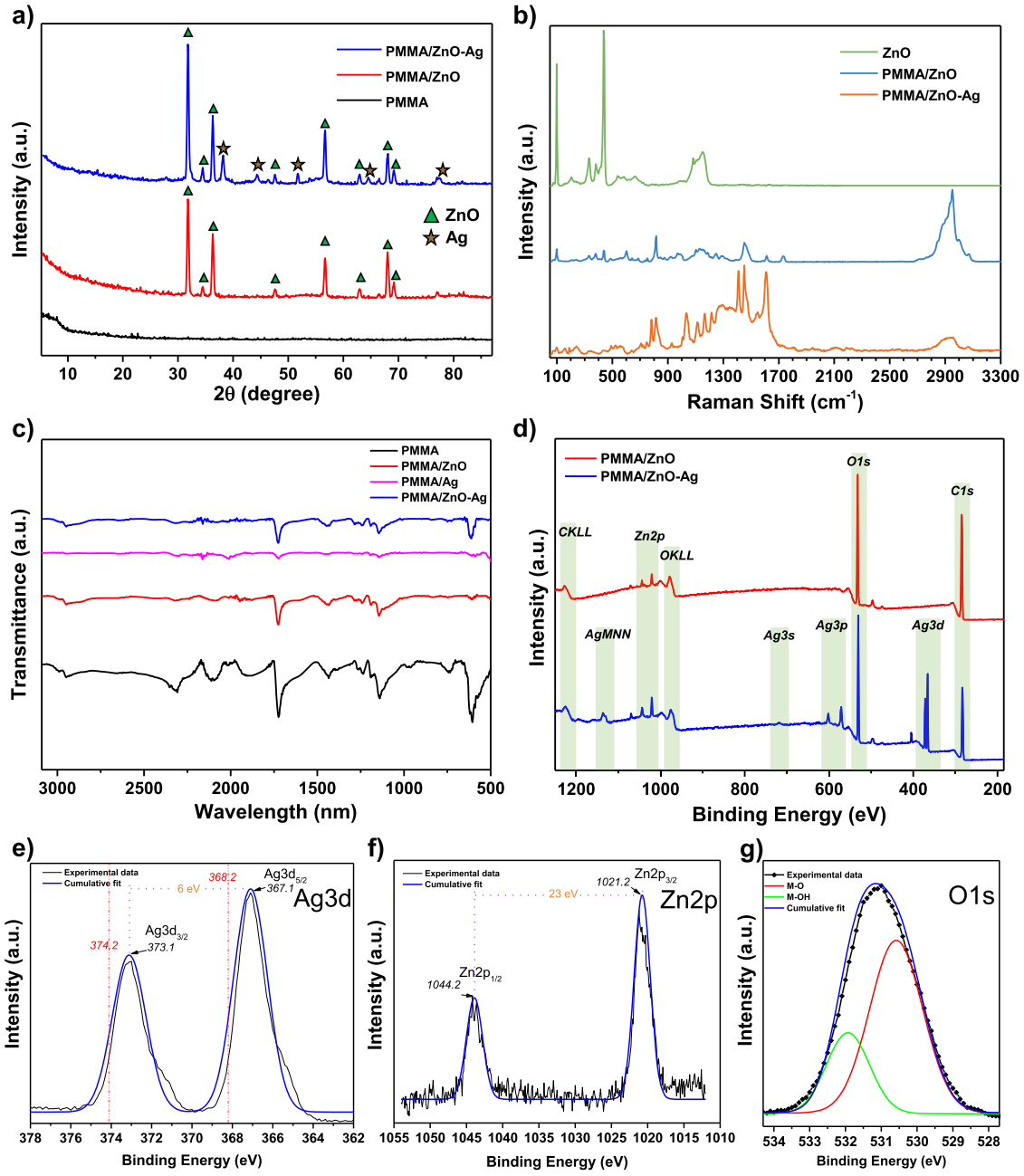


**Figure 3.** XRD, Raman, FT-IR, and XPS characterizations of fabricated PMMA NFs and their nanocomposites at concentrations of 6, 10, and 3% wt for PMMA NFs, ZnO nanorods, and Ag nanoparticles, respectively. (a) XRD patterns of pristine PMMA NFs, PMMA/ZnO NFs, and PMMA/ZnO−Ag NFs, (b) Raman spectra of pure ZnO nanorods and PMMA/ZnO and PMMA/ZnO−Ag NFs, (c) FT-IR studies of pristine PMMA NFs, PMMA/ZnO NFs, PMMA/Ag NFs, and PMMA/ZnO−Ag NFs, (d) survey XPS spectrum of PMMA/ZnO and PMMA/ZnO−Ag NFs, high-resolution regional XPS spectra of (e) Ag 3d, (f) Zn 2p, and (g) O 1s for PMMA/ZnO−Ag.

layer for 120 s. Diameter distribution of NFs and statistical data were analyzed via ImageJ. This process was carried out by examining randomly chosen 100 individual NFs taken from at least three SEM images of three different regions. The wettability character of NF mats was evaluated from high-speed camera images of an contact angle meter (Attension, Theta Lite). Static contact angle measurements were taken in different time intervals after placement of water droplets with a volume of 4 $\mu$L. Phase analysis, chemical composition, and molecular bond characteristics of the obtained PMMA, PMMA/Ag, PMMA/ZnO, and PMMA/ZnO−Ag NFs were characterized by using an X-ray diffractometer (Bruker AXS D8), energy-dispersive X-ray spectrometer (Bruker), and Fourier transform infrared spectrometer (PerkinElmer 400), respectively. Crystallinity and phase analyses were carried out using XRD (at $2\theta$ = 10−90°), Cu K$\alpha$ radiation ($\lambda$ = 1.540 Å) at a scanning rate of 0.1 step $s^{-1}$. To analyze bond characteristics, FT-IR measurements were performed over a range of 4000−400 $cm^{-1}$ by ATR mode. UV−visible spectroscopy (PerkinElmer Lambda 25) was performed in the wavelength range of 350−800 nm to monitor the photocatalytic degradation. The surface chemical composition of NFs was studied via X-ray photoelectron spectroscopy (XPS, Specs-Flex) using an XRm50 (UXC1000) source exciting radiation (1486.71 eV). All the binding energies were calibrated to the C 1s peak at 285.4 eV.

## 3. RESULTS AND DISCUSSION

This study proposes fabrication of multifunctional PMMA/ZnO−Ag NFs on mats for protective clothing applications.



https://dx.doi.org/10.1021/acsami.0c15606
ACS Appl. Mater. Interfaces 2021, 13, 5678−5690

Figure 1 presents the key steps of fabrication and the antibacterial, antiviral, self-cleaning, and sensing properties of the materials. First, a solution containing PMMA, ZnO nanorods, and Ag NPs was prepared. This solution was referred to as PMMA/ZnO−Ag. ZnO nanorods were synthesized using a hydrothermal method (Figure 1a) and Ag NPs were synthesized by the direct reduction of $AgNO_3$ in DMF. PMMA/ZnO−Ag electrospinning solutions were obtained after dissolution of PMMA and addition of ZnO nanorods to the Ag−DMF solution (Figure 1b). At the second step, the solution was electrospun on a mat (Figure 1c), which was later placed on the inner side of a fabric (Figure 1d). Multi-functional PMMA/ZnO−Ag NF mats were then studied through antimicrobial and antiviral test procedures (Figure 1e), photodegradation studies (Figure 1f), and SERS measurements (Figure 1g).

**3.1. Structural Properties of Multi-Functional NF Mats.** In this study, PMMA/ZnO−Ag NFs were electrospun on a mat. AgNPs were in situ synthesized by the reduction of $AgNO_3$ in DMF. The reducing mechanism of $Ag^+$ ions in DMF for the formation of AgNPs is known from previous studies.[13,19−21] For the case of hybrid nanocomposites containing ZnO nanorods, powders of ZnO nanorods were added to the PMMA solution. Additionally, Triton X-100 was used to prevent the agglomeration of ZnO particles. Uniform NFs without any beads were observed in all samples (Figure 2). The surface of PMMA NFs encrusted with AgNPs was relatively smooth and has a more homogeneous structure than NFs with ZnO nanorods. Synthesized AgNPs can be observed within the PMMA NF body and on ZnO nanorods (Figure 2d,f). One may notice that the surface of the NFs becomes rough by the incorporation of ZnO nanorods. This increase in the roughness suggests that ZnO nanorods were aligned not only inside the PMMA NFs but also on the surface of the fibers (Figure 2e,f). Such alignment of ZnO with other types of nanorods inside the NF body is probably due to magnetic and mechanic stimulation during electrospinning and such behavior has been reported in various studies.[22−26] For all samples, the distribution of the fiber diameter was analyzed (Figure 2g−i). The incorporation of Ag and ZnO NPs to the polymer solution broadened the distribution of the diameter and increased the fiber diameter. The average diameter and standard deviation for PMMA/Ag, PMMA/ZnO, and PMMA/ZnO−Ag NF mats were 371 ± 100, 457 ± 116, and 510 ± 122, respectively. The observed diameter differences of NPs, especially for ZnO rod containing them, were interpreted as the result of the raised polymer solution viscosity and favorably reducing the ion mobility and whipping instability during electrospinning.

The wetting properties of NF mats were evaluated by water contact angle measurements. As shown in Figure S1, while the PMMA NF mat exhibits a hydrophobic character with a water contact angle of about 120°, contact angles of PMMA/ZnO and PMMA/ZnO−Ag mats are immeasurable due to their highly hydrophilic behavior, where water droplets are adsorbed by mats completely in seconds.

The fabricated nanocomposite mats were analyzed by XRD, Raman, and FT-IR as presented in Figure 2. For revealing the crystalline and phase structures of the prepared nanocomposites, XRD patterns were measured and are shown in Figure 3a. No specific peaks have been observed for pure PMMA NFs, as expected from the amorphous polymer structure. Specifically, the 10 characteristic peaks at $2\theta$ = 31.8, 34.5, 36.3, 47.6, 56.7, 62.9, 66.5, 68.0, 69.2, and 77.0° are attributed to crystal planes (101), (002), (101), (102), (110), (103), (200), (112), (201), and (202), respectively, which is indexed to the hexagonal wurtzite phase of ZnO (JCPDS card no. 36-1451) in PMMA/ZnO and PMMA/ZnO−Ag NF mats.[27−29] The strong and narrow diffraction peaks in the pattern imply that the ZnO nanorods were of a high degree of crystallinity. Furthermore, the intensity shown for the (100) plane is higher than that of the (101) plane; this observation is a result of the rod-like structure of ZnO particles.[23,30] SEM images of ZnO given in Figure S2 further support this observation. Additional diffraction peaks for PMMA/ZnO−Ag NF mats correspond to $2\theta$ and crystalline planes of the cubic Ag crystal structure (JCPDS card no. 04-0783) of values 38.2°(111), 44.3°(200), 64.3°(220), and 77.5°(331). Except for ZnO and Ag, no other characteristic peaks have been observed in the XRD pattern that confirms the high purity of synthesized PMMA NF composites. The average crystallite sizes ($D$) of the Ag NPs and ZnO nanorods were evaluated using the Debye−Scherrer eq 6

$$D = \frac{0.9\lambda}{\beta \cos\theta} \tag{6}$$

In this equation,[31] $\lambda$, $\theta$, and $\beta$ are the wavelengths of X-ray radiation, Bragg's angle of the peaks, and the angular width of peaks at fwhm, respectively. The average crystal size of the ZnO nanorods was calculated as 23.39 nm.[32] The average crystallite size was 17.14 nm for Ag NPs. The absence of any additional peaks and shifts in the position of peaks suggest that Ag was not incorporated into the lattice of ZnO but was only present on the surface of ZnO.[33]

In Figure 3b, Raman spectra of the PMMA/ZnO−Ag NF mat and PMMA/ZnO and ZnO nanorods were observed. The vibration bands ascribed to ZnO nanoparticles were at 100 $cm^{-1}$ (low-wavenumber optical phonon E2 mode), 330 $cm^{-1}$ (second-order spectrum of ZnO), 380 $cm^{-1}$ (A1(T) optical phonon mode), 407 $cm^{-1}$ (E1(T) optical phonon mode), and 438 $cm^{-1}$ (E2 optical phonon band).[34] Additionally, the characteristic Raman band of PMMA occurred at 818 $cm^{-1}$ (the strong polarized band of PMMA) and 1456 $cm^{-1}$ [$\delta(\alpha$-$CH_3$) and $\delta$(O−$CH_3$)], and the region in the range 2900−3000 $cm^{-1}$ [$\nu(\alpha$-$CH_3$) and $\nu$(O−$CH_3$)] in the Raman spectra of the PMMA mats was decorated with ZnO nanorods.[35] To grasp additional evidence for the presence of Ag and ZnO nanorods in PMMA NFs, elemental analysis of the PMMA/ZnO−Ag NF mat was carried out by EDX mapping (Figure S3). In Figure 3c, FT-IR spectra of the PMMA/ZnO−Ag NF mat and PMMA/ZnO and ZnO nanorods are shown. The bands at around 1000 and 1150 $cm^{-1}$ are the specific absorption vibration peaks for PMMA. The two bands at 2950 and 2980 $cm^{-1}$ can be assigned to the −$CH_2$− and −$CH_3$ stretching vibrations, respectively. The band at around 680 $cm^{-1}$ is the specific absorption vibration peak for ZnO nanorods and after modification of the PMMA with AgNPs and ZnO nanorods, important changes are seen in the peak intensities.

The XPS analysis is carried out to investigate the surface chemical composition of NF mats, and the corresponding results are shown in Figure 3d−g. In the general survey spectra of NF mats, there are only C, Zn, and O peaks in PMMA/ZnO NFs. Additional Ag peaks are observed in PMMA/ZnO−Ag NFs. The presence of C might be caused by PMMA and the XPS instrument. The high-resolution spectrum of Ag, Zn, and


https://dx.doi.org/10.1021/acsami.0c15606
ACS Appl. Mater. Interfaces 2021, 13, 5678−5690

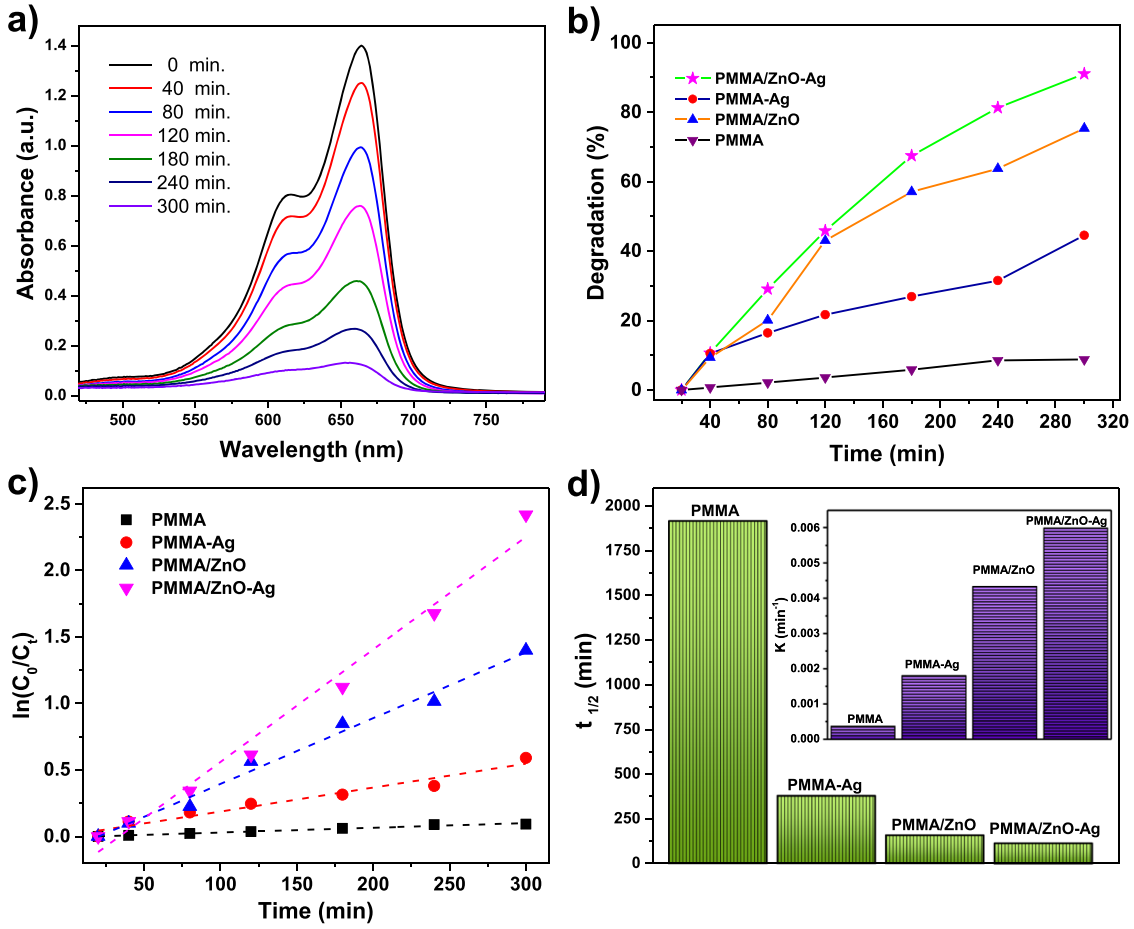


**Figure 4.** Photocatalytic activity of PMMA NF mats. (a) UV−vis absorbance of aqueous MB solution pipetted on PMMA/ZnO−Ag NFs over a time interval ranging from 0 to 300 min; ZnO and Ag NP concentration of 10 and 3% w/w, respectively. (b) Photocatalytic degradation (%) of MB on pure PMMA, PMMA/Ag NF, PMMA/ZnO, and PMMA/ZnO−Ag NF mats. (c) Plot of photocatalytic activity of NF mats as a function of time. (d) Half-life time of the photocatalytic degradation rate. The inset presents the pseudo-first-order reaction rate constant.

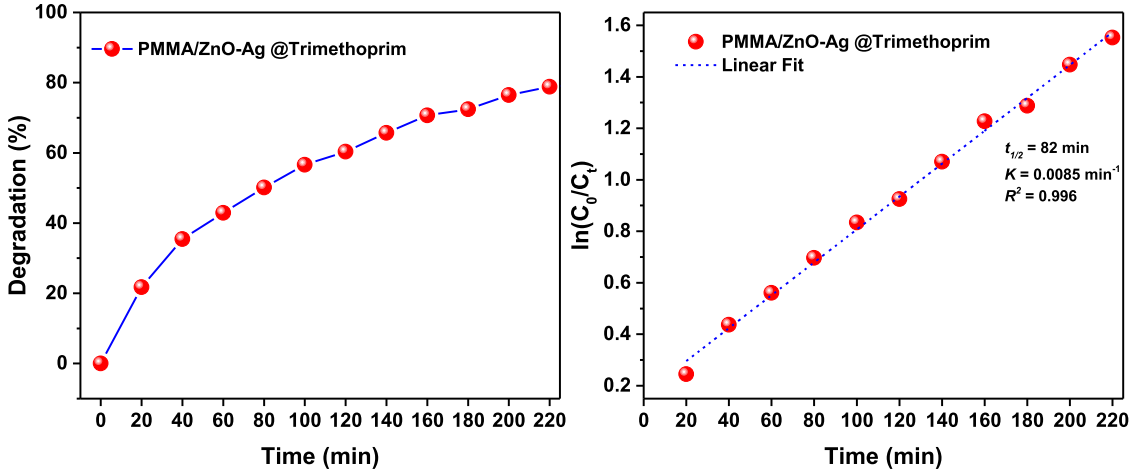


**Figure 5.** Photocatalytic degradation of trimethoprim by the PMMA/ZnO−Ag NF mat. HPLC-DAD chromatography showing the (a) degradation rate % and (b) kinetic plot of (ln $C_0/C_t$) of the photocatalytic degradation rate for trimethoprim. The inset data show the calculated values of pseudo-first-order reaction rate constant ($K$), $R$ squared value in regression ($R^2$), and half-life time ($t^{1/2}$).

O species obtained from the PMMA/ZnO−Ag NFs are shown in Figure 3d−g, respectively. The binding energy of Zn 2p peaks of 1044.2 and 1021.2 shown in Figure 3f are attributed to Zn $2p_{1/2}$ and Zn $2p_{3/2}$ eV with an orbit separation of 23 eV. These two peaks confirm that $Zn^{2+}$ ions form in ZnO nanorods.[36,37] As shown in Figure 3e, peaks of Ag $3d_{5/2}$ and Ag $3d_{3/2}$ located at 367.1 and 373.1 eV with spin orbit separation of 6 eV indicate that Ag embedded in PMMA NFs and on ZnO nanorods are in the form of metallic silver ($Ag^0$). Furthermore, the binding energies of Ag 3d shift to the lower



https://dx.doi.org/10.1021/acsami.0c15606
ACS Appl. Mater. Interfaces 2021, 13, 5678−5690

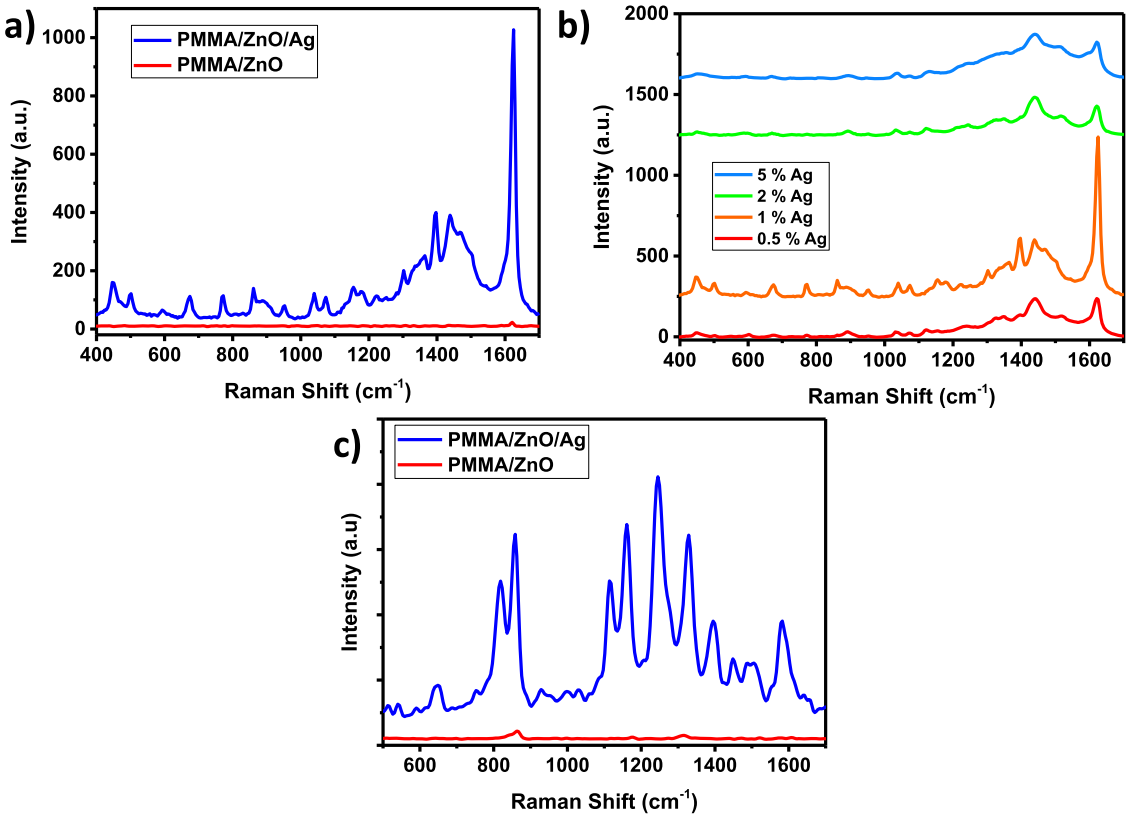


**Figure 6.** (a) SERS spectra of MB (1 mM) deposited on the PMMA/ZnO−Ag NF mat (blue line) and PMMA/ZnO NF mat (red line). (b) SERS spectra of MB (1 mM) on PMMA/ZnO−Ag NF mats loaded with different concentrations (0.5, 1, 3, and 5%) of AgNPs, ordered from bottom to top. (c) SERS spectra of 4-nitrophenol (1 mM) deposited on the PMMA/ZnO−Ag NF mat (blue line) and the PMMA/ZnO NF mat (red line).

binding energy compared with bare metallic Ag (368.2 and 374.2 eV for Ag $3d_{5/2}$ and Ag $3d_{3/2}$), respectively.[38] In good agreement with previous works, this lower energy shifting (about 1.1 eV) of the Ag 3d region is attributed to the interaction between Ag nanoparticles and ZnO nanorods, which leads to the adjustment of their corresponding Fermi levels to the same value.[39−42] In Figure 3g, the O 1s profile can be fitted to two peaks at 530.5 and 532 eV. These peaks indicate two different kinds of O species in ZnO. They can be associated with the lattice oxygen (M−O) and chemisorbed O of the surface hydroxyls (M−OH).[43] To check the release of any nanoparticles and molecules from NF mats, we performed releasing experiments with NFs incubated in water from 1 to 7 h and the UV−vis absorbance spectra of aqueous solution were taken. Results given in Figure S4 show that no characteristic peaks of Ag NPs, ZnO nanorods, and trace DMF molecules were determined in a duration between 1 and 7 h.

**3.2. Photocatalytic Performance of PMMA/ZnO−Ag NFs.** The photocatalytic activity of the fabricated NF mats of pure PMMA, PMMA nanocomposite with presynthesized Ag nanoparticles in DMF medium (PMMA/Ag), PMMA nanocomposite with ZnO rod-like nanoparticles synthesized by the hydrothermal method (PMMA/ZnO), and PMMA nanocomposite with ZnO and Ag (PMMA/ZnO−Ag NFs) NPs were evaluated using photodegradation of the MB solution, as shown in Figure 4. PMMA NFs with ZnO and AgNPs illustrated the highest photodegradation efficiency for MB. In Figure 4a, the intensity of the characteristic absorbance peak (664 cm) of MB was decreasing over the time interval of 0−300 min. The findings demonstrated that after 300 min of degradation, 91% of MB dye was degraded; however, for PMMA/ZnO and PMMA/Ag, these values were 75 and 44.5%, respectively (Figure 5b). For pure PMMA, the degradation was not noticeable (8.8%) and until the end of 300 min there was no explicit photocatalytic activity. The plot of $\ln(C_0/C)$ as a function of time (Figure 4c) for the as-prepared material was represented as a linear regression with a slope equivalent to the apparent pseudo-first-order rate constant $k$ ($min^{-1}$) (Figure 4d) and the half-life time was also calculated using eq 4. It was shown from calculations that the half-life time and rate constant for PMMA/ZnO−Ag, PMMA/ZnO, and PMMA/Ag were 115 min and 0.00599 $min^{-1}$, 160 min and 0.0043 $min^{-1}$, 380 min and 0.0018 $min^{-1}$, respectively. Results showed that the incorporation of the PMMA body with both ZnO nanorods and Ag NPs shows improved activity due to the efficient charge separation of the ZnO−Ag composite relative to pure ZnO and Ag. The synergetic activity of ZnO−Ag structures on catalytic activity is well known.[44] When the PMMA/ZnO−Ag NF mats are irradiated by UV light with a photon energy higher than the band gap of ZnO (5.2 eV), electrons ($e^-$) transfer to the conduction band (CB) from the valence band (VB), leaving the same amount of photogenerated holes ($h^+$) in the VB. The photoexcited electrons can transfer from the ZnO nanorods to the CB of AgNPs (4.27 eV), which is narrower than CB of ZnO. Electrons accumulated at Ag NPs or the CB of ZnO can be transferred to oxygen molecules adsorbed on the surface to form free oxygen radicals, such as $^{\bullet}O^{2-}$, $^{\bullet}HO_2$, and $^{\bullet}OH$, while the photoinduced holes react with surface-bound water molecules to produce $^{\bullet}OH$ radicals. These radicals are strong oxidants for the mineralization of MB.[28,41,44−46]



https://dx.doi.org/10.1021/acsami.0c15606
ACS Appl. Mater. Interfaces 2021, 13, 5678−5690

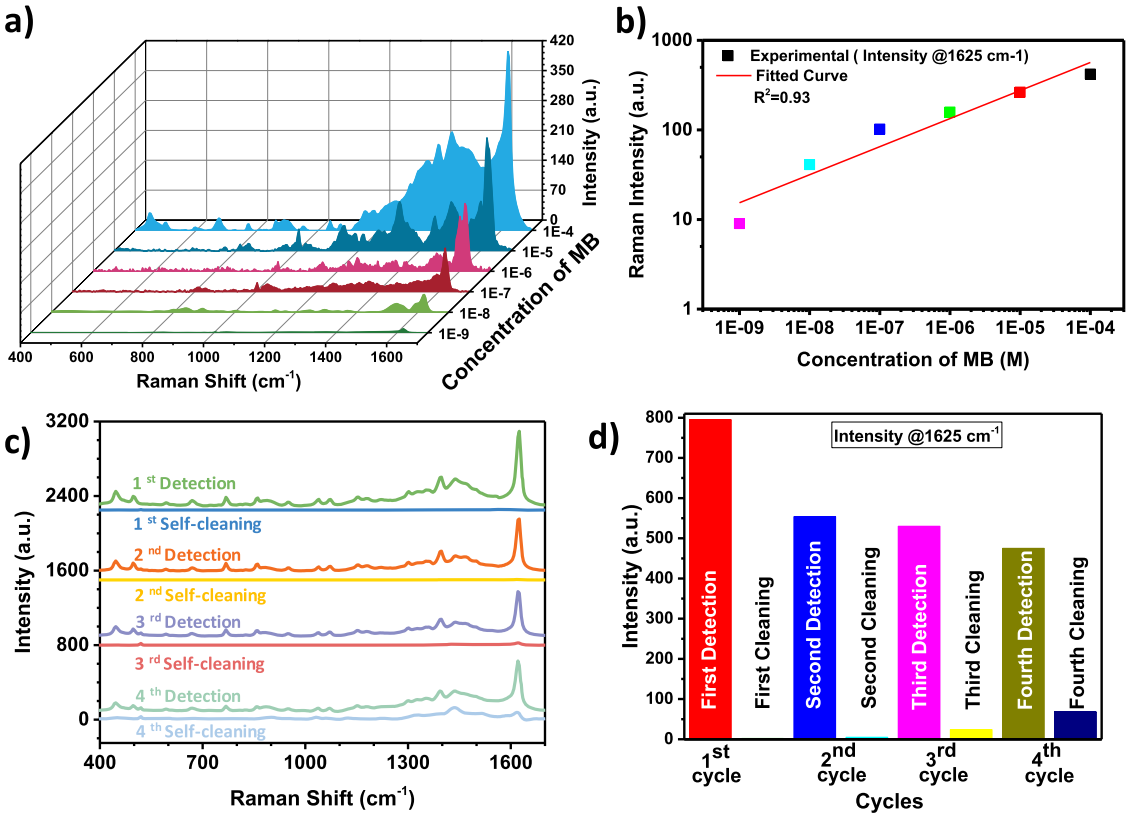


**Figure 7.** (a) SERS spectra of different concentrations of MB (from 100 $\mu$M to 1 nM) probed on the PMMA/ZnO−Ag NF mat. (b) SERS intensity as a function of the concentration of MB. (c) SERS spectra of MB (2 $\mu$L, 1 mM) drop-cast on the PMMA/ZnO−Ag NF mat. The mat was self-cleaned using UV-irradiation for 45 min before being reused for four cycles. (d) Variation of the SERS signal intensity at 1625 $cm^{-1}$ with the increasing number of self-cleaning cycles.

Furthermore, the photocatalytic degradation performance of the PMMA/ZnO−Ag NF mat was evaluated by monitoring the degradation rate of trimethoprim by using HPLC-DAD (Figure 5). Trimethoprim is an antibiotic commonly used for the treatment of a broad range of bacterial infections, including gastro, respiratory, and urinary infections in both human and veterinary medicine.[47,48] However, it is highly water-soluble and resistant to biodegradable processes, so it can easily leak and accumulate in aquatic resources.[49] Trimetrophim has been detected in domestic and industrial wastewater.[50,51] As with other antibiotics, toxicologic concerns of trimetroprim motivate the development of new catalytic materials and systems. The results showed that the concentration of trimetrophim (20 $mg{\cdot}mL^{-1}$) and its characteristic peak amplitude decreased with the increase of the irradiation time. About 80% of the trimetrophim degraded at the end of 220 min. One-half of the initial concentration of trimethoprim was destroyed throughout an interval not higher than 80 min. Moreover, the kinetic plot shows that the calculated regression values for the trimethoprim are close to unity, which proves that the photocatalytic degradation reaction followed the pseudo-first-order kinetics.

To demonstrate the concept of using NFs in protective clothing applications, we investigated photocatalytic degradation of 4-nitrophenol, as a representative air pollutant. Nitrophenols are among the most important and versatile industrial organic compounds and are widely used in the chemical industry and are listed as priority pollutants by the U.S. Environmental Protection Agency (EPA) and World Health Organization (WHO). Beside the aquatic environment, 4-nitrophenol is also an air pollutant that exists in the atmospheric environment.[52−55] As the result given in Figure S5, the concentration and characteristic peak amplitude of 4-nitrophenol decreased by increasing the irradiation time. About 52% of the 4-nitrophenol was degraded at the end of 300 min. One-half of the initial concentration of 4-nitrophenol was destroyed in about 230 min.

**3.3. SERS Performance of PMMA/ZnO−Ag NFs.** The nanostructured material with an Ag-rich composition offers a highly suitable and flexible platform for SERS-based trace-level quantitative detection. The SERS spectra of MB are shown in Figure 6a. There is a substantial difference between the intensity of signals measured using NF mats in the presence and absence of AgNPs (Figure 6a). These results suggest that AgNPs facilitate plasmonic hot spots that effectively concentrate electromagnetic fields at/near the metallic surfaces and increase the signal amplitude by several orders of magnitude.[56,57] To understand the effect of Ag NP concentration on the SERS activity, the Raman spectrum was measured after a 1 mM MB analyte molecule was dropped on NF mats prepared using different Ag loadings. As shown in Figure 6b, the highest intensity of the SERS spectrum of MB was obtained after utilizing of a NF with 1 wt %. Ag. The higher the concentration of AgNPs (>1 wt %), for example, 3 and 5 wt %, the lower the SERS signals detected. This result is probably due to the aggregation of Ag nanostructures resembling bulk-like behavior.[58] The close-placement of Ag nanoparticles within the NF at increased Ag loadings was further evidenced with STEM images presented in Figure S6. To further demonstrate the SERS performance of our platform, we studied an air


https://dx.doi.org/10.1021/acsami.0c15606
ACS Appl. Mater. Interfaces 2021, 13, 5678−5690

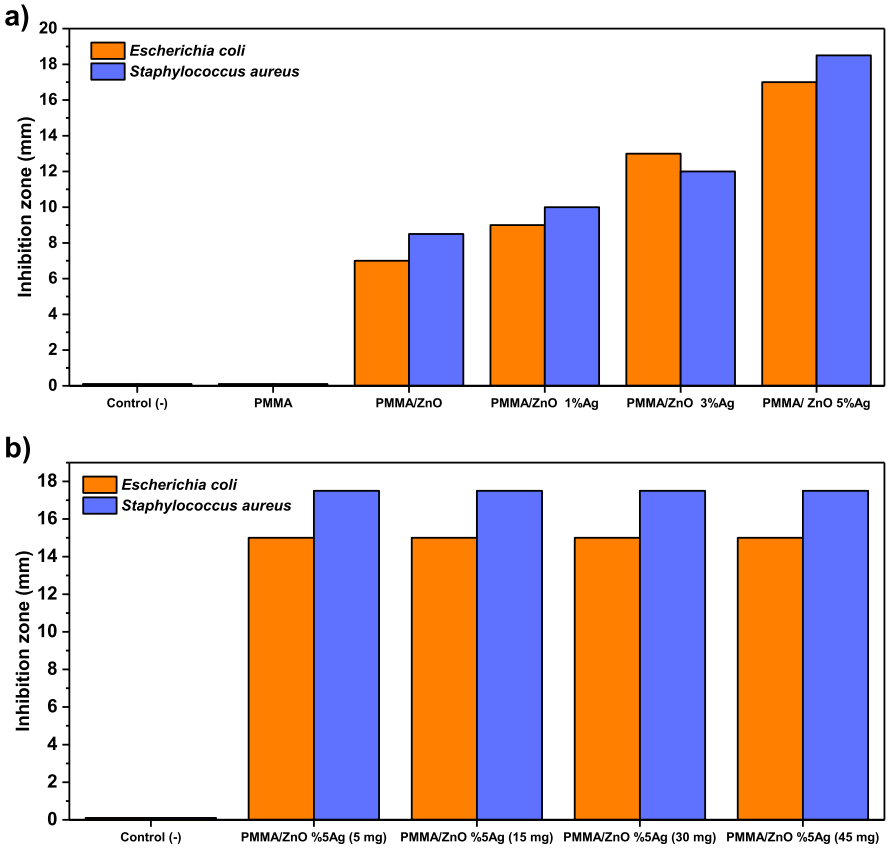


**Figure 8.** Antibacterial activity of NF mats; (a) antibacterial activity of different types and different Ag concentrations of NF mats; (b) antibacterial activity of different amounts of PMMA/ZnO-5% Ag NF mats.

pollutant, 4-nitrophenol, as a probe molecule. The results presented in Figure 6c show Raman spectra of 4-nitrophenol on the NF mat in the presence and absence of Ag NPs.

Regarding the SERS performance, it is critical to calculate the limit of detection, which is an important figure of merit for ultra-trace quantitative detection capability. Thus, SERS activity was measured on PMMA/ZnO−Ag NFs using series of MB concentrations that range from 100 $\mu$M to 1 nM. The characteristic peak of MB at 1625 $cm^{-1}$ could be observed at a concentration as low as 1 nM (Figure 7a). The calculation of AEF is also considered as an important parameter for evaluating the performance of SERS platforms. The calculated AEF (eq 1) was 6.43 × $10^5$ with $I_{SERS}$ (9 counts), $I_{RM}$ (14 counts), $C_{SERS}$ (1 nM), and $C_{RM}$ (1 mM). This value was comparable considering previous studies.[12,59] A quantitative analytical calibration curve was plotted in Figure 7b with a coefficient of determination ($R^2$) of 0.93.

"An important capability of our platform is self-cleaning enabled by the photocatalytic activity of the materials. In an effort to demonstrate the resuability of the fabricated mats, PMMA/ZnO−Ag NFs were self-cleaned via the UV radiation in an aqueous medium. After the self-cleaning process, SERS measurement was repeated. This procedure was successively repeated for four cycles. The results showed that our material can be usable for four times by application of photocatalytic cleaning process. As shown in Figure 7c,d, the self-cleaning process continued effectively until the fourth cycle, without significant reduction in the SERS activity. These results suggested repeated use of the mats and retainment of their sensing capabilities." (Section 3.3.) Future studies may further improve the durability using different fabrics, whose structure has a strong effect on the stability of the deposited nanomaterials.[60]

**3.4. Antimicrobial Activity of Electrospun PMMA/ZnO−Ag NFs.** The in vitro antimicrobial activity of PMMA/ZnO−Ag NF mats was qualitatively assessed by the presence/absence of inhibition zones. As a result, PMMA/ZnO−Ag NF mats elucidated a promising antibacterial impact against both *E. coli* and *S. aureus* with their respective diameter zones of inhibition of 7−17 and 8.5−18.5 mm. Depending on the result of the agar diffusion method, *S. aureus* was the most susceptible microorganism, which was strongly inhibited by PMMA/ZnO−Ag NFs and the inhibition zone was ∼18.5 mm (Figure 8a). Also effect of the amount of PMMA/ZnO−Ag NFs on antibacterial effect was evaluated. The results showed that the antibacterial activity did not show a significant change with varying amounts (5, 15, 30, and 45 mg) of the material. Within the range of investigated conditions, the inhibition zone was 15 ± 2 and 17.5 ± 1 mm against *E. coli* and *S. aureus*, respectively (Figure 8b). This observation is likely a result of the surface area of the NFs that comes into contact with bacteria remaining the same. The possible antimicrobial mechanism of PMMA/ZnO−Ag NFs is generation of ROS that affect the bacterial membrane, causing intracellular components to leak and damage to protein/DNA, leading to the death of the bacteria.

**3.5. Antiviral Activity of Electrospun PMMA/ZnO−Ag NFs.** The average $TCKID_{50}$ values of the test repeats were evaluated for contact with coronavirus (BCV) and para-influenzavirus (BPIV3) using a PMMA/ZnO−Ag NF mat. In


https://dx.doi.org/10.1021/acsami.0c15606
ACS Appl. Mater. Interfaces 2021, 13, 5678−5690

the case of a control sample without NFs and nanomaterials, no significant titer regression ($V_b$) was observed for both viruses (log 0.25 for 1 h and log 1.75 for 24 h). The observed antiviral activities ($M_v$ = log $V_b$ − log $V_c$) of the NF against BCV and BPIV3 were 3.75 and 1.75, respectively, for 1 h; 4.25 and 4, respectively, for 24 h (Table 1). After 1 h of contact of the mat and BCV, the virus titer 3.75 log declined, while after 24 h the 4.25 log decreased. For Mat-BPIV3, the $M_v$ value was observed as 1.5 log and 4 log, respectively.

**Table 1. Values of Virus Titers and Evaluation of Antiviral Activity of PMMA/ZnO−Ag NFs against BCoV and BPIV3**

| titration values of viruses[a] ($\log_{10}$ TCKID$_{50}$/100 mL) | | |
|---|---|---|
| | contact time | |
| sample | 1 h | 24 h |
| control (BCV) (log $V_b$) | 7.75 | 6.25 |
| control (BPIV3) (log $V_b$) | 7.75 | 6.25 |
| NF mat (BCV) (log $V_c$) | 4.00 | 2.00 |
| NF mat (BPIV3) (log $V_c$) | 6.25 | 2.25 |
| Antiviral Performance ($M_v$ = log $V_b$ − log $V_c$) | | |
| NF mat (BCV) | 3.75 | 4.25 |
| NF mat (BPIV3) | 1.50 | 4.00 |

[a]Average value of three test repeats.

One way to evaluate the antiviral activity of antiviral agents is the logarithmic decrease value in the control titer (if 3.0 > [$M_v$] ≥ 2.0, effective; if [$M_v$] ≥ 3.0, very effective) at the end of the specified incubation period. NF mats showed excellent antiviral performance against both the viruses in the long term (24 h). For the short term (1 h), NF mats were ineffective against the influenza virus, indicating that ZnO has a specific effect on BCV. It is likely due to the specific interaction properties of $Zn^{2+}$ ions released from ZnO nanorods embedded in NFs with corona viruses. Cell culture studies have demonstrated that $Zn^{2+}$ effectively inhibits activity of enveloped positive strand RNA (RNA+) nidoviruses, which includes major human and livestock corona viruses such SARS-COV and also COVID-19.[5,6,61,62] Zn is a major ligand of ACE2 spike. The inhibition mechanism of $Zn^{2+}$ ions on coronaviruses is briefly based on targeting the activity of viral RNA-dependent RNA polymerase (RdRp), which is the core enzyme of their multi-protein replication and transcription complex.

## 4. CONCLUSIONS

In summary, this study has presented a multi-functional material with strong potential for use in protective clothing applications. The inherently flexible electrospun NF-based platform was decorated with two types of semiconductor and metallic nanoparticles to provide antibacterial, antiviral, photocatalytic-mediated self-cleaning and SERS-based sensing characteristics. The simple, entirely solution-processable, and inexpensive fabrication approach could be readily adapted to different applications. Besides the synergetic combination of different properties, the presented platform displayed remarkable performance in each of these characteristics. Probe molecules could be detected via SERS at concentrations as low as 1 nM and the recyclable photocatalytic degradation efficiencies reached 90%. From the findings, the presented material showed significant antibacterial activity against both *E. coli* and *S. aureus* as a result of combined use of both ZnO and Ag nanostructures. Antiviral activity of the platform against the coronavirus and the parainfluenza virus further highlights the strong promise of these mats for protective clothing applications. Altogether, our platform offers passive and active strategies against infection with microbial agents. Antibacterial and antiviral characteristics provide passive protection, and photocatalytic degradation offers the ability to clean after contamination with agents. SERS-based sensing opens up possibilities for diagnosis and analysis of the contamination. The nonwoven and flexible nature of electrospun NFs is critically advantageous for integration of these materials into mats. The findings and concepts presented in this study motivate development of multi-functional material platforms against pandemics such as the COVID-19.

## ■ ASSOCIATED CONTENT

### Supporting Information

The Supporting Information is available free of charge at https://pubs.acs.org/doi/10.1021/acsami.0c15606.

Evaluation of wettability characteristics, additional SEM images, EDX, UV−visible absorbance spectra; and details of photocatalytic studies (PDF)

## ■ AUTHOR INFORMATION


### Corresponding Author

**Erkan Yilmaz** − *ERNAM−Erciyes University Nanotechnology Application and Research Center, Kayseri 38039, Turkey; Faculty of Pharmacy and Technology Research & Application Center (TAUM), Erciyes University, Kayseri 38039, Turkey; ChemicaMed Chemical Inc., Erciyes University Technology Development Zone, Kayseri 38039, Turkey;* orcid.org/0000-0001-8962-3199; Email: erkanyilmaz@erciyes.edu.tr

### Authors

**Sultan Karagoz** − *ERNAM−Erciyes University Nanotechnology Application and Research Center, Kayseri 38039, Turkey; Department of Textile Engineering, Faculty of Engineering, Erciyes University, Kayseri 38039, Turkey*

**N. Burak Kiremitler** − *ERNAM−Erciyes University Nanotechnology Application and Research Center, Kayseri 38039, Turkey; Department of Materials Science and Engineering, Faculty of Engineering, Erciyes University, Kayseri 38039, Turkey*

**Gokhan Sarp** − *ERNAM−Erciyes University Nanotechnology Application and Research Center, Kayseri 38039, Turkey; Faculty of Pharmacy, Erciyes University, Kayseri 38039, Turkey*

**Sami Pekdemir** − *ERNAM−Erciyes University Nanotechnology Application and Research Center, Kayseri 38039, Turkey; Department of Materials Science and Engineering, Faculty of Engineering, Erciyes University, Kayseri 38039, Turkey*

**Samaa Salem** − *ERNAM−Erciyes University Nanotechnology Application and Research Center, Kayseri 38039, Turkey; Faculty of Pharmacy, Erciyes University, Kayseri 38039, Turkey*

**Ayşe Gencay Goksu** − *Department of Virology, Faculty of Veterinary Medicine, Erciyes University, Kayseri 38039, Turkey*

**M. Serdar Onses** − *ERNAM−Erciyes University Nanotechnology Application and Research Center, Kayseri 38039, Turkey; Department of Materials Science and*




https://dx.doi.org/10.1021/acsami.0c15606
ACS Appl. Mater. Interfaces 2021, 13, 5678−5690

*Engineering, Faculty of Engineering, Erciyes University, Kayseri 38039, Turkey;* orcid.org/0000-0001-6898-7700

**Ibrahim Sozdutmaz** − *Department of Virology, Faculty of Veterinary Medicine, Erciyes University, Kayseri 38039, Turkey*

**Ertugrul Sahmetlioglu** − *ERNAM−Erciyes University Nanotechnology Application and Research Center, Kayseri 38039, Turkey; Safiye Cikrikcioglu Vocational School, Kayseri University, Kayseri 38039, Turkey; ChemicaMed Chemical Inc., Erciyes University Technology Development Zone, Kayseri 38039, Turkey*

**Ergun Samet Ozkara** − *ERNAM−Erciyes University Nanotechnology Application and Research Center, Kayseri 38039, Turkey*

**Ahmet Ceylan** − *Faculty of Pharmacy, Erciyes University, Kayseri 38039, Turkey*

Complete contact information is available at: https://pubs.acs.org/10.1021/acsami.0c15606

### Notes

The authors declare no competing financial interest.

## ■ ACKNOWLEDGMENTS

We are grateful for the financial support of the Unit of the Scientific Research Projects of Erciyes University (FBA-2019-8697) and Turkish scholarship (Türkiye Bursları) for funding this work.

## ■ REFERENCES

(1) Feng, S.; Shen, C.; Xia, N.; Song, W.; Fan, M.; Cowling, B. J. Rational Use of Face Masks in the COVID-19 Pandemic. *Lancet Respir. Med.* **2020**, *8*, 434−436.

(2) Greenhalgh, T.; Schmid, M. B.; Czypionka, T.; Bassler, D.; Gruer, L. Face Masks for the Public during the Covid-19 Crisis. *BMJ* **2020**, *369*, m1435.

(3) Gavade, N. L.; Kadam, A. N.; Babar, S. B.; Gophane, A. D.; Garadkar, K. M.; Lee, S.-W. Biogenic synthesis of gold-anchored ZnO nanorods as photocatalyst for sunlight-induced degradation of dye effluent and its toxicity assessment. *Ceram. Int.* **2020**, *46*, 11317−11327.

(4) Ghaffari, H.; Tavakoli, A.; Moradi, A.; Tabarraei, A.; Bokharaei-Salim, F.; Zahmatkeshan, M.; Farahmand, M.; Javanmard, D.; Kiani, S. J.; Esghaei, M.; Pirhajati-Mahabadi, V.; Ataei-Pirkooh, A.; Monavari, S. H. Inhibition of H1N1 Influenza Virus Infection by Zinc Oxide Nanoparticles: Another Emerging Application of Nanomedicine. *J. Biomed. Sci.* **2019**, *26*, 70.

(5) Skalny, A. V.; Rink, L.; Ajsuvakova, O. P.; Aschner, M.; Gritsenko, V. A.; Alekseenko, S. I.; Svistunov, A. A.; Petrakis, D.; Spandidos, D. A.; Aaseth, J.; Tsatsakis, A.; Tinkov, A. A. Zinc and Respiratory Tract Infections: Perspectives for CoviD'19 (Review). *Int. J. Mol. Med.* **2020**, *46*, 17−26.

(6) Kumar, A.; Kubota, Y.; Chernov, M.; Kasuya, H. Potential Role of Zinc Supplementation in Prophylaxis and Treatment of COVID-19. *Med. Hypotheses* **2020**, *144*, 109848.

(7) Hong, D.; Cao, G.; Qu, J.; Deng, Y.; Tang, J. Antibacterial Activity of $Cu_2O$ and Ag Co-Modified Rice Grains-like ZnO Nanocomposites. *J. Mater. Sci. Technol.* **2018**, *34*, 2359−2367.

(8) Aggrawal, S.; Mandal, T. K.; Mohanty, P. $Ag^+$ Driven Antimicrobial Activity of $Ag^+$: ZnO Nanowires Immobilized on Paper Matrices. *Materialia* **2019**, *8*, 100490.

(9) Liu, Q.; Liu, E.; Li, J.; Qiu, Y.; Chen, R. Rapid Ultrasonic-Microwave Assisted Synthesis of Spindle-like Ag/ZnO Nanostructures and Their Enhanced Visible-Light Photocatalytic and Antibacterial Activities. *Catal. Today* **2020**, *339*, 391−402.

(10) Lungu, M.-V.; Vasile, E.; Lucaci, M.; Pătroi, D.; Mihăilescu, N.; Grigore, F.; Marinescu, V.; Brătulescu, A.; Mitrea, S.; Sobetkii, A.; Sobetkii, A. A.; Popa, M.; Chifiriuc, M.-C. Investigation of Optical, Structural, Morphological and Antimicrobial Properties of Carboxymethyl Cellulose Capped Ag-ZnO Nanocomposites Prepared by Chemical and Mechanical Methods. *Mater. Charact.* **2016**, *120*, 69−81.

(11) Wang, Y.; Zhang, Q.; Zhang, C.-l.; Li, P. Characterisation and Cooperative Antimicrobial Properties of Chitosan/Nano-ZnO Composite Nanofibrous Membranes. *Food Chem.* **2012**, *132*, 419−427.

(12) Pekdemir, S.; Torun, I.; Sakir, M.; Ruzi, M.; Rogers, J. A.; Onses, M. S. Chemical Funneling of Colloidal Gold Nanoparticles on Printed Arrays of End-Grafted Polymers for Plasmonic Applications. *ACS Nano* **2020**, *14*, 8276−8286.

(13) Karagoz, S.; Kiremitler, N. B.; Sakir, M.; Salem, S.; Onses, M. S.; Sahmetlioglu, E.; Ceylan, A.; Yilmaz, E. Synthesis of Ag and $TiO_2$ Modified Polycaprolactone Electrospun Nanofibers (PCL/$TiO_2$-Ag NFs) as a Multifunctional Material for SERS, Photocatalysis and Antibacterial Applications. *Ecotoxicol. Environ. Saf.* **2020**, *188*, 109856.

(14) Langer, J.; Jimenez de Aberasturi, D.; Aizpurua, J.; Alvarez-Puebla, R. A.; Auguié, B.; Baumberg, J. J.; Bazan, G. C.; Bell, S. E. J.; Boisen, A.; Brolo, A. G.; Choo, J.; Cialla-May, D.; Deckert, V.; Fabris, L.; Faulds, K.; García de Abajo, F. J.; Goodacre, R.; Graham, D.; Haes, A. J.; Haynes, C. L.; Huck, C.; Itoh, T.; Käll, M.; Kneipp, J.; Kotov, N. A.; Kuang, H.; Le Ru, E. C.; Lee, H. K.; Li, J. F.; Ling, X. Y.; Maier, S. A.; Mayerhöfer, T.; Moskovits, M.; Murakoshi, K.; Nam, J. M.; Nie, S.; Ozaki, Y.; Pastoriza-Santos, I.; Perez-Juste, J.; Popp, J.; Pucci, A.; Reich, S.; Ren, B.; Schatz, G. C.; Shegai, T.; Schlücker, S.; Tay, L. L.; Thomas, K. G.; Tian, Z. Q.; Van Duyne, R. P.; Vo-Dinh, T.; Wang, Y.; Willets, K. A.; Xu, C.; Xu, H.; Xu, Y.; Yamamoto, Y. S.; Zhao, B.; Liz-Marzán, L. M. Present and future of surface-enhanced Raman scattering. *ACS Nano* **2020**, *14*, 28−117.

(15) Oxford, J. S.; Lambkin, R.; Guralnik, M.; Rosenbloom, R. A.; Petteruti, M. P.; DiGian, K.; LeFante, C. Preclinical in Vitro Activity of QR-435 against Influenza a Virus as a Virucide and in Paper Masks for Prevention of Viral Transmission. *Am. J. Therapeut.* **2007**, *14*, 455−461.

(16) Ramakrishnan, M. A. Determination of 50% Endpoint Titer Using a Simple Formula. *World J. Virol.* **2016**, *5*, 85.

(17) Alahmad, W. R.; Alawi, M. A. Photocatalytic Degradation of Diclofenac and Ibuprofen from Simulated Wastewater Using $SiO_2$-$TiO_2$- (Ru,N) by Artificial Light. *Fresenius Environ. Bull.* **2016**, *25*, 4299.

(18) Li, C.; Yu, J.; Xu, S.; Jiang, S.; Xiu, X.; Chen, C.; Liu, A.; Wu, T.; Man, B.; Zhang, C. Constructing 3D and Flexible Plasmonic Structure for High-Performance SERS Application. *Adv. Mater. Technol.* **2018**, *3*, 1800174.

(19) Pastoriza-Santos, I.; Liz-Marzán, L. M. Synthesis of Silver Nanoprisms in DMF. *Nano Lett.* **2002**, *2*, 903−905.

(20) Pastoriza-Santos, I.; Liz-Marzán, L. M. Formation and Stabilization of Silver Nanoparticles through Reduction by N,N-Dimethylformamide. *Langmuir* **1999**, *15*, 948−951.

(21) Zhang, Y.; Shi, R.; Yang, P. Synthesis of Ag Nanoparticles with Tunable Sizes Using N,N-Dimethyl Formamide. *J. Nanosci. Nanotechnol.* **2014**, *14*, 3011−3016.

(22) Bashouti, M.; Salalha, W.; Brumer, M.; Zussman, E.; Lifshitz, E. Alignment of Colloidal CdS Nanowires Embedded in Polymer Nanofibers by Electrospinning. *ChemPhysChem* **2006**, *7*, 102−106.

(23) Nain, R.; Jassal, M.; Agrawal, A. K. Polymeric Nanofiber Composites with Aligned ZnO Nanorods. *Compos. Sci. Technol.* **2013**, *86*, 9−17.

(24) Nain, R.; Singh, D.; Jassal, M.; Agrawal, A. K. Zinc Oxide Nanorod Assisted Rapid Single-Step Process for the Conversion of Electrospun Poly(Acrylonitrile) Nanofibers to Carbon Nanofibers with a High Graphitic Content. *Nanoscale* **2016**, *8*, 4360−4372.

(25) Roskov, K. E.; Kozek, K. A.; Wu, W.-C.; Chhetri, R. K.; Oldenburg, A. L.; Spontak, R. J.; Tracy, J. B. Long-Range Alignment of Gold Nanorods in Electrospun Polymer Nano/Microfibers. *Langmuir* **2011**, *27*, 13965−13969.

(26) Zhang, C.-L.; Lv, K.-P.; Hu, N.-Y.; Yu, L.; Ren, X.-F.; Liu, S.-L.; Yu, S.-H. Macroscopic-Scale Alignment of Ultralong Ag Nanowires in Polymer Nanofiber Mat and Their Hierarchical Structures by Magnetic-Field-Assisted Electrospinning. *Small* **2012**, *8*, 2936−2940.
(27) Deng, Q.; Duan, X.; Ng, D. H. L.; Tang, H.; Yang, Y.; Kong, M.; Wu, Z.; Cai, W.; Wang, G. Ag Nanoparticle Decorated Nanoporous ZnO Microrods and Their Enhanced Photocatalytic Activities. *ACS Appl. Mater. Interfaces* **2012**, *4*, 6030−6037.
(28) Pimpliskar, P. V.; Motekar, S. C.; Umarji, G. G.; Lee, W.; Arbuj, S. S. Synthesis of Silver-Loaded ZnO Nanorods and Their Enhanced Photocatalytic Activity and Photoconductivity Study. *Photochem. Photobiol. Sci.* **2019**, *18*, 1503−1511.
(29) Shan, G.; Zheng, S.; Chen, S.; Chen, Y.; Liu, Y. Multifunctional ZnO/Ag Nanorod Array as Highly Sensitive Substrate for Surface Enhanced Raman Detection. *Colloids Surf., B* **2012**, *94*, 157−162.
(30) Cheng, B.; Samulski, E. T. Hydrothermal Synthesis of One-Dimensional ZnO Nanostructures with Different Aspect Ratios. *Chem. Commun.* **2004**, *4*, 986−987.
(31) Cullity, B. D.; Graham, C. D. *Introduction to Magnetic Materials*; John Wiley & Sons, 2008,
(32) Jayram, N. D.; Sonia, S.; Poongodi, S.; Kumar, P. S.; Masuda, Y.; Mangalaraj, D.; Ponpandian, N.; Viswanathan, C. Superhydrophobic Ag decorated ZnO nanostructured thin film as effective surface enhanced Raman scattering substrates. *Appl. Surf. Sci.* **2015**, *355*, 969−977.
(33) Sakir, M.; Salem, S.; Sanduvac, S. T.; Sahmetlioglu, E.; Sarp, G.; Onses, M. S.; Yilmaz, E. Photocatalytic green fabrication of Au nanoparticles on ZnO nanorods modified membrane as flexible and photocatalytic active reusable SERS substrates. *Colloids Surf., A* **2020**, *585*, 124088.
(34) Korepanov, V. I.; Chan, S. Y.; Hsu, H. C.; Hamaguchi, H. O. Phonon Confinement and Size Effect in Raman Spectra of ZnO Nanoparticles. *Heliyon* **2019**, *5*, No. e01222.
(35) Willis, H. A.; Zichy, V. J. I.; Hendra, P. J. The Laser-Raman and Infra-Red Spectra of Poly(Methyl Methacrylate). *Polymer* **1969**, *10*, 737−746.
(36) Ziashahabi, A.; Prato, M.; Dang, Z.; Poursalehi, R.; Naseri, N. The effect of silver oxidation on the photocatalytic activity of Ag/ZnO hybrid plasmonic/metal-oxide nanostructures under visible light and in the dark. *Sci. Rep.* **2019**, *9*, 11839.
(37) Yıldırım, Ö. A.; Unalan, H. E.; Durucan, C. Highly efficient room temperature synthesis of silver-doped zinc oxide (ZnO: Ag) nanoparticles: structural, optical, and photocatalytic properties. *J. Am. Ceram. Soc.* **2013**, *96*, 766−773.
(38) Moulder, J. F.; Stickle, W. F.; Sobol, P. E.; Bomben, K. D. *Handbook of X-ray Photo Electrospectroscopy: A Reference Book of Standard Spectra for Identification and Interpretation of XPS Data*, Physical Electronics, Reissue edition; Physical Electronics: USA 18725, Lakedrive East, Chanhassen, MN 55317, 1995.
(39) Lu, F.; Wang, J.; Chang, Z.; Zeng, J. Uniform deposition of Ag nanoparticles on ZnO nanorod arrays grown on polyimide/Ag nanofibers by electrospinning, hydrothermal, and photoreduction processes. *Mater. Des.* **2019**, *181*, 108069.
(40) Liang, Y.; Guo, N.; Li, L.; Li, R.; Ji, G.; Gan, S. Facile synthesis of Ag/ZnO micro-flowers and their improved ultraviolet and visible light photocatalytic activity. *New J. Chem.* **2016**, *40*, 1587−1594.
(41) Zheng, Y.; Zheng, L.; Zhan, Y.; Lin, X.; Zheng, Q.; Wei, K. Ag/ZnO heterostructure nanocrystals: synthesis, characterization, and photocatalysis. *Inorg. Chem.* **2007**, *46*, 6980−6986.
(42) Gu, C.; Cheng, C.; Huang, H.; Wong, T.; Wang, N.; Zhang, T.-Y. Growth and photocatalytic activity of dendrite-like ZnO@ Ag heterostructure nanocrystals. *Cryst. Growth Des.* **2009**, *9*, 3278−3285.
(43) Abliz, A.; Huang, C.-W.; Wang, J.; Xu, L.; Liao, L.; Xiao, X.; Wu, W.-W.; Fan, Z.; Jiang, C.; Li, J.; Guo, S.; Liu, C.; Guo, T. Rational design of ZnO: H/ZnO bilayer structure for high-performance thin-film transistors. *ACS Appl. Mater. Interfaces* **2016**, *8*, 7862−7868.
(44) Kandula, S.; Jeevanandam, P. Sun-Light-Driven Photocatalytic Activity by ZnO/Ag Heteronanostructures Synthesized via a Facile Thermal Decomposition Approach. *RSC Adv.* **2015**, *5*, 76150−76159.
(45) Lin, D.; Wu, H.; Zhang, R.; Pan, W. Enhanced Photocatalysis of Electrospun Ag-ZnO Heterostructured Nanofibers. *Chem. Mater.* **2009**, *21*, 3479−3484.
(46) Raji, R.; Sibi, K. S.; Gopchandran, K. G. ZnO:Ag Nanorods as Efficient Photocatalysts: Sunlight Driven Photocatalytic Degradation of Sulforhodamine B. *Appl. Surf. Sci.* **2018**, *427*, 863−875.
(47) Burchall, J. J. Trimethoprim and Pyrimethamine. *Mechanism of Action of Antimicrobial and Antitumor Agents*; Springer Berlin Heidelberg, 1975; Vol. 304−320.
(48) De Paula, F. C. C. R.; De Pietro, A. C.; Cass, Q. B. Simultaneous Quantification of Sulfamethoxazole and Trimethoprim in Whole Egg Samples by Column-Switching High-Performance Liquid Chromatography Using Restricted Access Media Column for on-Line Sample Clean-Up. *J. Chromatogr. A* **2008**, *1189*, 221−226.
(49) Göbel, A.; McArdell, C.; Joss, A.; Siegrist, H.; Giger, W. Fate of Sulfonamides, Macrolides, and Trimethoprim in Different Wastewater Treatment Technologies. *Sci. Total Environ.* **2007**, *372*, 361−371.
(50) Watkinson, A. J.; Murby, E. J.; Kolpin, D. W.; Costanzo, S. D. The Occurrence of Antibiotics in an Urban Watershed: From Wastewater to Drinking Water. *Sci. Total Environ.* **2009**, *407*, 2711−2723.
(51) Li, B.; Zhang, T. Mass Flows and Removal of Antibiotics in Two Municipal Wastewater Treatment Plants. *Chemosphere* **2011**, *83*, 1284−1289.
(52) Boehncke, A.; Koennecker, G.; Mangelsdorf, I.; Wibbertmann, A. *Concise International Chemical Assessment Document 20—Mononitrophenols*; World Health Organization: Geneva, 2000.
(53) Harrison, M. A. J.; Barra, S.; Borghesi, D.; Vione, D.; Arsene, C.; Iulian Olariu, R. Nitrated phenols in the atmosphere: a review. *Atmos. Environ.* **2005**, *39*, 231−248.
(54) Delhomme, O.; Morville, S.; Millet, M. Seasonal and diurnal variations of atmospheric concentrations of phenols and nitrophenols measured in the Strasbourg area, France. *Atmos. Pollut. Res.* **2010**, *1*, 16−22.
(55) Tremp, J.; Mattrel, P.; Fingler, S.; Giger, W. Phenols and nitrophenols as tropospheric pollutants: emissions from automobile exhausts and phase transfer in the atmosphere. *Water, Air, Soil Pollut.* **1993**, *68*, 113−123.
(56) Karabel Ocal, S.; Pekdemir, S.; Serhatlioglu, M.; Ipekci, H. H.; Sahmetlioglu, E.; Narin, I.; Duman, F.; Elbuken, C.; Demirel, G.; Onses, M. S. Eco-Friendly Fabrication of Plasmonically Active Substrates Based on End-Grafted Poly(Ethylene Glycol) Layers. *ACS Sustainable Chem. Eng.* **2019**, *7*, 4315−4324.
(57) Sakir, M.; Pekdemir, S.; Karatay, A.; Küçüköz, B.; Ipekci, H. H.; Elmali, A.; Demirel, G.; Onses, M. S. Fabrication of Plasmonically Active Substrates Using Engineered Silver Nanostructures for SERS Applications. *ACS Appl. Mater. Interfaces* **2017**, *9*, 39795−39803.
(58) Li, X.; Chen, G.; Yang, L.; Jin, Z.; Liu, J. Multifunctional Au-Coated $TiO_2$ Nanotube Arrays as Recyclable SERS Substrates for Multifold Organic Pollutants Detection. *Adv. Funct. Mater.* **2010**, *20*, 2815−2824.
(59) Martín, A.; Wang, J. J.; Iacopino, D. Flexible SERS Active Substrates from Ordered Vertical Au Nanorod Arrays. *RSC Adv.* **2014**, *4*, 20038−20043.
(60) Celik, N.; Altındal, S.; Gozutok, Z.; Ruzi, M.; Onses, M. S. Effect of fabric texture on the durability of fluorine-free superhydrophobic coatings. *J. Coat. Technol. Res.* **2020**, *17*, 785.
(61) Te Velthuis, A. J. W.; van den Worm, S. H. E.; Sims, A. C.; Baric, R. S.; Snijder, E. J.; van Hemert, M. J. $Zn^{2+}$ Inhibits Coronavirus and Arterivirus RNA Polymerase Activity in Vitro and Zinc Ionophores Block the Replication of These Viruses in Cell Culture. *PLoS Pathog.* **2010**, *6*, No. e1001176.
(62) Read, S. A.; Obeid, S.; Ahlenstiel, C.; Ahlenstiel, G. The Role of Zinc in Antiviral Immunity. *Adv. Nutr.* **2019**, *10*, 696−710.


https://dx.doi.org/10.1021/acsami.0c15606
*ACS Appl. Mater. Interfaces* 2021, 13, 5678−5690